Astronomy & Astrophysics

N₂H⁺ depletion in the massive protostellar cluster AFGL 5142

G. Busquet[1], R. Estalella[1], Q. Zhang[2], S. Viti[3], A. Palau[4], P. T. P. Ho[2,5], and Á. Sánchez-Monge[1]

[1] Departament d'Astronomia i Meteorologia (IEEC-UB), Institut de Ciències del Cosmos, Universitat de Barcelona, Martí i Franquès 1, 08028 Barcelona, Catalunya, Spain
e-mail: gbusquet@am.ub.es

[2] Harvard-Smithsonian Center for Astrophysics, Cambridge, MA, 02138, UK

[3] Department of Physics and Astronomy, University College London, Grower Street, London WC1E 6BT, UK

[4] Institut de Ciències de l'Espai (CSIC-IEEC), Campus UAB, Facultat de Ciències, Torre C-5 parell, 08193 Bellaterra, Catalunya, Spain

[5] Academia Sinica Institute of Astronomy and Astrophysics, Taipei, Taiwan

ABSTRACT

Aims. We aim at investigating the NH₃/N₂H⁺ abundance ratio toward the high-mass star-forming region AFGL 5142 with high angular resolution in order to study whether the NH₃/N₂H⁺ ratio behaves similarly to the low-mass case, for which the ratio decreases from starless cores to cores associated with young stellar objects (YSOs).

Methods. CARMA was used to observe the 3.2 mm continuum and N₂H⁺ (1–0) emission toward AFGL 5142. We used NH₃ (1, 1) and (2, 2), as well as HCO⁺ (1–0) and H¹³CO⁺ (1–0) data available from the literature, to study the chemical environment. Additionally, we performed a time-dependent chemical modeling of the region.

Results. The 3.2 mm continuum emission reveals a dust condensation of ∼23 $M_\odot$ associated with the massive YSOs, deeply embedded in the strongest NH₃ core (hereafter central core). The dense gas emission traced by N₂H⁺ reveals two main cores, the western core of ∼0.08 pc in size and the eastern core of ∼0.09 pc, surrounded by a more extended and complex structure of ∼0.5 pc, mimicking the morphology of the NH₃ emission. The two cores are located to the west and to the east of the 3.2 mm dust condensation. Toward the central core the N₂H⁺ emission drops significantly, indicating a clear chemical differentiation in the region. The N₂H⁺ column density in the central core is one order of magnitude lower than in the western and eastern cores. Furthermore, we found low values of the NH₃/N₂H⁺ abundance ratio ∼50–100 toward the western and eastern cores and high values up to 1000 associated with the central core. The chemical model used to explain the differences seen in the NH₃/N₂H⁺ ratio indicates that density along with temperature is a key parameter in determining the abundances of both NH₃ and N₂H⁺. The high density ($n \simeq 10^6$ cm⁻³) and temperature ($T \simeq 70$ K) reached in the central core allow molecules such as CO to evaporate from grain mantles. The CO desorption causes a significant destruction of N₂H⁺, which favors the formation of HCO⁺. This result is supported by our observations, which show that N₂H⁺ and HCO⁺ are anticorrelated in the central core. The observed values of the NH₃/N₂H⁺ ratio in the central core can be reproduced by our model for times of $t \simeq 4.5-5.3 \times 10^5$ yr, while in the western and eastern cores the NH₃/N₂H⁺ ratio can be reproduced by our model for times in the range $10^4-3 \times 10^6$ yr.

Conclusions. The NH₃/N₂H⁺ abundance ratio in AFGL 5142 does not follow the same trend as in regions of low-mass star formation mainly because of the high temperature reached in hot cores.

Key words. astrochemistry – stars: formation – ISM: individual objects: AFGL 5142 – ISM: clouds – ISM: molecules – ISM: abundances

1. Introduction

It is well known that *N*-bearing molecules, such as NH₃ and N₂H⁺, are excellent tracers of the interstellar dense gas because none of these molecules deplete onto dust grains until densities reach ∼10⁶ cm⁻³ (Bergin & Langer 1997; Tafalla et al. 2004; Flower et al. 2006). Thus observations of these dense gas tracers have become a powerful tool when studying the sites of star formation. However, only a few observational studies have focused on comparing NH₃ and N₂H⁺ cores, and these studies, which were carried out toward low-mass star-forming regions, find that the NH₃/N₂H⁺ abundance ratio is around 60–90 close to the young stellar objects (YSOs), while it rises to 140–190 in starless cores (Caselli et al. 2002a; Hotzel et al. 2004; Friesen et al. 2010). In the intermediate-mass cores surrounding the high-mass star IRAS 20293+3952, Palau et al. (2007) find the same trend, with a high NH₃/N₂H⁺ ratio, up to 300, in the cores with starless properties, and around 50 for the cores associated with YSOs,

clearly showing that chemical differentiation is important in the region. All these studies show that the NH₃/N₂H⁺ abundance ratio is consistent with being a "chemical clock".

To investigate the behavior of the NH₃/N₂H⁺ abundance ratio in high-mass star-forming regions and see if the NH₃/N₂H⁺ ratio in massive YSOs shows the same trend as in the low-mass regime, we carried out observations and chemical modeling of the high-mass star-forming region AFGL 5142, located at a distance of 1.8 kpc (Snell et al. 1988) in the Perseus arm. The region was selected as a good candidate for studying the NH₃/N₂H⁺ ratio because the high angular resolution NH₃ emission reveals several dense cores, which have very different temperatures, and one of them is associated with star formation in clustered mode with the presence of hot cores.

The region consists of two main centers of high-mass star formation in different evolutionary stages. The brightest near-infrared source (Hunter et al. 1995) IRAS 05274+3345, with a

bolometric luminosity of $3.8 \times 10^3 \, L_\odot$ (Carpenter et al. 1990), lies near the western edge of the NH_3 gas (Estalella et al. 1993) and a lack of dense gas emission associated with it suggests that the IRAS source is a more evolved region, which is consistent with detection of optical nebulosity (Eiroa et al. 1994). Based on its position in the J vs. $J - H$ diagram, Chen et al. (2005) classify the IRAS source as a B2 star of 3 Myr. Torrelles et al. (1992) detect a faint radio continuum source, IRAS 05274+3345 East (hereafter referred as AFGL 5142), about 30″ to the east of the IRAS source, which coincides with the peak position of the dust emission at 3.4 mm (Hunter et al. 1999) and the NH_3 emission peak (Estalella et al. 1993). Assuming that the centimeter emission arises from an optically thin H II region, the flux density is equivalent to a zero-age main sequence (ZAMS) star of spectral type B2 or earlier (Torrelles et al. 1992; Hunter et al. 1995) with a luminosity of $4 \times 10^3 \, L_\odot$.

In the near-infrared, Hunter et al. (1995) report a cluster of 28 embedded sources in a region of 1′ (~0.3 pc in radius) near the position of the radio continuum source. Recently, Qiu et al. (2008) carried out Spitzer Space Telescope IRAC and MIPS observations toward AFGL 5142. The authors identify 44 YSOs, 20 of them clustered around the central massive star and surrounded by a more extended and sparse distribution of young stars and protostars. In addition, high angular resolution observations of maser emission reveal a cluster of H_2O and CH_3OH masers in an area of ~5″ (Hunter et al. 1995; Goddi & Moscadelli 2006; Goddi et al. 2007). Subsequent observations with the very large array (VLA) in the A configuration at 8.4 GHz and with the submillimeter array (SMA) at 1.2 mm with ~1″ of angular resolution were carried out by Zhang et al. (2007), who find that the centimeter source is resolved into three peaks, and that the 3.4 mm source detected by Hunter et al. (1999) actually consists of five millimeter sources. Regarding the molecular outflow emission in this region, Zhang et al. (2007) identify three molecular outflows in CO (2–1) and SO 6_5-5_4, one of them coinciding with an HCO^+ outflow and the well-collimated SiO jet detected by Hunter et al. (1999). All three outflows appear to originate from the dust condensation in a region of about 3″. All this information indicates that active star formation in clustered mode is taking place in AFGL 5142.

The dense gas emission in this region has been studied with single-dish telescopes in NH_3, CS, HCN, HCO^+, CH_3OH, and CH_3CN (Verdes-Montenegro et al. 1989; Estalella et al. 1993; Hunter et al. 1995, 1999; Cesaroni et al. 1999). In particular, the dense gas emission traced by the NH_3 molecule has been observed with high angular resolution using the VLA (Zhang et al. 2002). The high angular resolution NH_3 emission consists of a central and compact core associated with the dust condensation, harboring at least three intermediate/high-mass young stars, surrounded by fainter NH_3 cores located in a more extended structure with no signs of stellar activity (either maser nor molecular outflow emission associated with it) indicating that the region may harbor cores in different evolutionary stages. The presence of cores containing massive star(s), together with cores with no star-formation activity, makes this region a good choice for studying how the NH_3/N_2H^+ ratio behaves in high-mass star-forming regions.

In this paper we report CARMA observations of the continuum emission at 3.2 mm and the dense gas traced by N_2H^+ (1–0) toward AFGL 5142. The paper layout is as follows. In Sect. 2 we summarize our observations and the data reduction process. In Sect. 3 we present the main results for the continuum and N_2H^+ molecular line emission. In Sect. 4 we analyze the molecular emission of several species by computing their column density

maps. In Sect. 5 we show the main results of the chemical model to qualitatively reproduce the abundances of the region. Finally, in Sect. 6 we discuss our findings, and we list the main conclusions in Sect. 7.

2. Observations

The Combined Array for Research in Millimeter-wave Astronomy[1] (CARMA) was used to observe the 3.2 mm continuum and the N_2H^+ (1–0) emission toward AFGL 5142. CARMA consists of six 10 m and nine 6 m antennas located at 2200 m elevation at Cedar Flat in the Inyo Mountains of California. The observations were carried out on 2007 February 4 and March 11 using the array in the C configuration with 14 antennas in the array. The projected baselines ranged from 26 to 370 m. The phase center was set at $\alpha = 05^h 30^m 48\overset{s}{.}02$, $\delta = +33°47'54\overset{''}{.}47$. The $FWHM$ of the primary beam at the frequency of the observations was 132″ for the 6 m antennas and 77″ for the 10 m antennas. System temperatures were around 250 K during both days.

The digital correlator was configured to observe simultaneously the continuum emission and the N_2H^+ (1–0) group of the hyperfine transitions (93.176331 GHz, in the lower sideband). The continuum data were recorded in two ~500 MHz bands covering the frequency ranges 93.44–93.88 GHz and 96.74–97.18 GHz from the receiver lower and upper sidebands, respectively. We used two consecutive bands of 8 MHz of bandwidth with 63 channels in each band, providing a spectral resolution of 0.42 km s^{-1} to observe the N_2H^+ (1–0) emission.

Phase calibration was performed with the quasars 0530+135 and 0555+398, with typical rms in the phases of 12° and 8°, respectively. The absolute position accuracy was estimated to be around 0″.1. Flux and bandpass calibration was set by using 3C84. Data were calibrated and imaged using the standard procedures in MIRIAD (Sault et al. 1995). We combined the data from both days of observations. The rms in the naturally weighted maps is ~0.7 mJy beam^{-1} in the continuum, and ~55 mJy beam^{-1} per 0.42 km s^{-1} channel in the line data. The synthesized beam of the continuum image is 2″.53 × 1″.71, PA = 68.8°. For the line emission, which is more extended than the continuum, we applied a uv-taper function of 52 kλ (3″.5 in the image plane) to improve the signal-to-noise ratio and to recover the extended emission. The resulting synthesized beam is 4″.04 × 3″.53, with PA = 79.1°. The continuum and N_2H^+ emissions were cleaned using a box around the emitting region.

3. Results

3.1. Continuum emission

Figure 1 presents the continuum map at 3.2 mm. We detected a single millimeter peak associated with IRAS 05274+3345 East (we could not resolve the two main 1.2 mm peaks MM-1 and MM-2, separated by about 1″, detected with the SMA by Zhang et al. 2007). The millimeter continuum emission has a single compact peak component with a flux density of 107.1 ± 1.6 mJy, surrounded by a more extended and flattened emission elongated
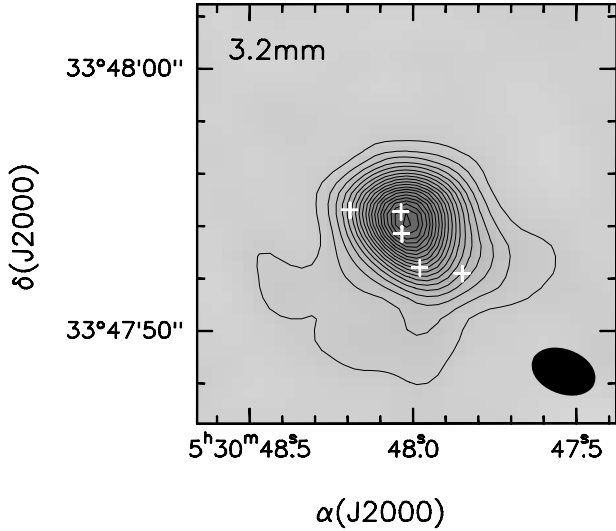
Fig. 1. 3.2 mm continuum emission toward AFGL 5142. Contour levels range from 3 to 60σ in steps of 3σ, where σ is the rms of the map, 0.7 mJy beam^{-1}. The synthesized beam, shown in the bottom right corner, is 2$\farcs$53 $\times$ 1$\farcs$71, PA = 68.8°. White crosses indicate the millimeter sources detected by Zhang et al. (2007) at 1.2 mm with the SMA.

in the west and southeast directions. A 2D Gaussian fit to the compact component yields a deconvolved size of 2$\farcs$9 $\times$ 2$\farcs$3, PA = 16.5° (5200 AU at the distance of the source). The peak position is α(J2000) = 05^{h}30^{m}48^{s}01; δ(J2000) = +33°47′54$\farcs$1. The total flux density when taking into account the extended emission is 126.4 $\pm$ 3.1 mJy, in very good agreement with the flux density at 88 GHz reported by Hunter et al. (1999), which is ~125 mJy. Assuming that the dust emission is optically thin, and using the dust opacity law of Hildebrand (1983), with a dust emissivity index of $\beta = 1$ (see Zhang et al. 2007, for a description of its derivation), and for a dust temperature of 45 K (based on the estimation of Hunter et al. 1999) the total mass of dust and gas from thermal continuum emission is 23 $M_\odot$ (after correcting for the expected contribution, ~4%, from the ionized gas; see Hunter et al. 1999). This mass is consistent with the mass estimated from the 1 mm SMA observations (~21 $M_\odot$). Although Zhang et al. (2007) report a mass of 50 $M_\odot$, the difference arises from the value adopted for the dust emissivity index, $\beta = 1.5$ instead of 1. There is a factor of 4 in the uncertainty of the mass, mainly due to uncertainties in the dust opacity and the dust emissivity index.

3.2. Molecular line emission: N$_2$H$^+$

In Fig. 2 we show the N$_2$H$^+$ (1–0) spectra not corrected for the primary beam response at some selected positions of AFGL 5142, and in Table 1 we present the line parameters obtained from the fit of the hyperfine spectra toward these positions. Figure 3 presents the velocity channel maps for the N$_2$H$^+$ (1–0) emission toward AFGL 5142. The channel with maximum intensity for the hyperfine component $F_1F = 01 \rightarrow$ 12 was found at the velocity v= −3.5 km s^{-1}. The systemic velocity of the cloud is v_{LSR} = −3 km s^{-1}.

The zero-order moment map integrated for all the hyperfine transitions is presented in Fig. 4a. For comparison, we also show (in Fig. 4b) the NH$_3$ (1, 1) integrated intensity map from Zhang et al. (2002) overlaid with the cluster of infrared sources reported in recent studies (Hunter et al. 1995; Chen et al. 2005; Qiu et al. 2008) in order to have a complete view of the stellar content in
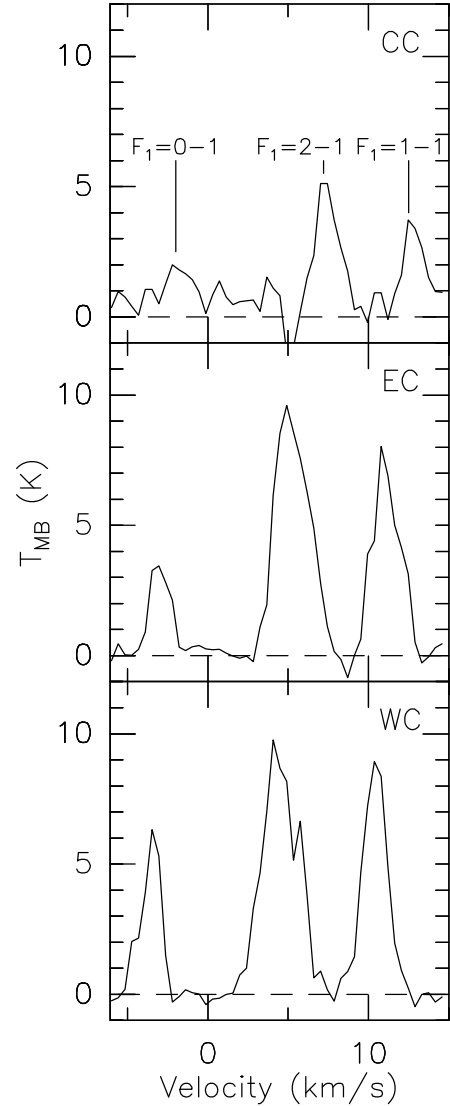

Fig. 2. N$_2$H$^+$ (1–0) spectra toward three positions of AFGL 5142. The three positions labeled on each panel are, *from top to bottom*, CC (NH$_3$ peak or central core), EC (peak of the eastern core), and WC (peak of the western core, see Fig. 4).

AFGL 5142. The overall structure of the integrated N$_2$H$^+$ (1–0) emission consists of two main cores, located to the west and to the east of the dust condensation (hereafter western and eastern cores), surrounded by a more extended structure with an X-shape morphology, roughly following the same morphology as the NH$_3$ emission. As can be seen in Fig. 4, the western core seems to contain at least one infrared source embedded in the dense gas, located close to the position of the NH$_3$ peak, and it displays typical characteristics of protostars (Chen et al. 2005), whereas the infrared source lying close to the peak position of the eastern core has no associated infrared excess and has been classified as a Herbig Ae/Be or T Tauri star (Chen et al. 2005). However, there is no clear evidence that these infrared sources are really associated with the dense gas. Additionally, since the sensitivity of Spitzer observations is ~1 $M_\odot$ (Qiu et al. 2008) and that of near-infrared studies is ~0.2–0.4 $M_\odot$ (Chen et al. 2005), we cannot discard the possibility of more infrared sources embedded in the dense gas. A 2D Gaussian fit to the western and eastern cores yields deconvolved sizes of ~9$\farcs$3 $\times$ 7$\farcs$6 (~0.08 $\times$ 0.07 pc) and ~10$\farcs$4 $\times$ 8$\farcs$3 (~0.09 $\times$ 0.07 pc), respectively. Interestingly,

Table 1. Parameters of the hyperfine fits to the N_2H^+ (1–0) line for the central position of each core.

| Core | Position[a] | | $A\tau_m$[b] | v_{LSR}[c] | Δv | τ_m[d] | T_{ex} | $N(N_2H^+)$ |
	α(J2000)	δ(J2000)	(K km s^{-1})	(km s^{-1})	(km s^{-1})		(K)	($\times 10^{12}$ cm^{-2})
central[e]	05:30:48.02	33:47:53.4	0.51 ± 0.04	–0.97 ± 0.06	1.11 ± 0.10	0.10 ± 0.03	8.2 ± 1.6	2.8 ± 0.9
eastern	05:30:48.73	33:47:52.9	1.35 ± 0.02	–2.92 ± 0.01	1.60 ± 0.02	0.10 ± 0.02	16.7 ± 1.1	18.5 ± 1.2
western	05:30:47.47	33:47:51.7	2.45 ± 0.01	–3.57 ± 0.01	1.31 ± 0.03	0.27 ± 0.02	12.4 ± 0.8	14.4± 1.2

Notes. [a] Positions, given in (h m s) and (° ′ ″); [b] $A = f(J_\nu(T_{ex}) - J_\nu(T_{bg}))$, where f is the filling factor (assumed to be 1), T_{ex} is the excitation temperature of the transition, T_{bg} is the background radiation temperature, and $J_\nu(T)$ is the intensity in units of temperature, $J_\nu(T) = (h\nu/k)/(\exp(h\nu/kT) - 1)$; [c] v_{LSR} corresponding to the $F_1F = 01 \rightarrow 12$ hyperfine component; [d] optical depth of the main line, $F_1F = 23 \rightarrow 12$, obtained from the fit; [e] position of the central core taken from the NH_3 emission peak.

toward the dust condensation where the intermediate/high-mass stars are deeply embedded in the strongest and compact NH_3 core (hereafter central core), the N_2H^+ emission decreases drastically. However, the central core is detected in N_2H^+ in some velocity channels from 7 km s^{-1} to 8.7 km s^{-1}, and its peak positions is slightly shifted to the east ($\sim$2″) from the dust and NH_3 peaks.

We used the hyperfine component $F_1F = 01 \rightarrow 12$ to study the kinematics of the N_2H^+ emission seen from Fig. 3 since this hyperfine component is strong and not blended with the other hyperfine components. In Fig. 5a we show the first-order moment map (intensity weighted mean v_{LSR}), and in Fig. 5b the second-order map (intensity weighted velocity dispersion) for this hyperfine component.

The first-order moment map shows that the eastern and western cores appear at different velocities (see also the channel maps shown in Fig. 3). Toward the eastern core there is a small velocity gradient in the east-west direction from $\sim$−3.5 km s^{-1} to $\sim$−1.8 km s^{-1}. On the other hand, the western core shows a velocity gradient from $\sim$−4.7 km s^{-1} to $\sim$−2.6 km s^{-1} with increasing velocities from the southwest to the northeast. In fact, as can be seen in Fig. 5b, the emission from the western core has very broad lines, with a velocity dispersion of $\sim$0.8– 1 km s^{-1}, which corresponds for a Gaussian line profile, to a $FWHM$ of $2\sqrt{2\ln 2} \times \sigma_v$, where σ_v is the velocity dispersion of $\sim$1.8–2.3 km s^{-1} (corrected for instrumental resolution) at the eastern side of the western core. This region of broad emission coincides with the passage of outflow B of Zhang et al. (2007). The values around $\sim$2 km s^{-1} are significantly higher than the thermal line width $\sim$0.2–0.3 km s^{-1} (estimated for a kinetic temperature of 25 K and 45 K, respectively), indicative of N_2H^+ having a significant contribution from nonthermal processes, such as turbulence injected by the molecular outflows, and/or global systematic motions. Regarding the eastern core, the typical value found for the velocity dispersion is in the range $\sim$0.3–0.5 km s^{-1}, corresponding to line widths of $\sim$0.2–1.1 km s^{-1} (corrected for instrumental resolution). In addition, there is a clumpy cavity structure toward the northwest clearly visible in the −2.6 and −2.2 km s^{-1} channel maps of Fig. 3, which appear redshifted by $\sim$1 km s^{-1} with respect to the systemic velocity.

In Fig. 6a we present the position-velocity (PV) plot made across the east-west direction (PA = 90°), encompassing the N_2H^+ peaks of the western and eastern cores, which clearly shows a ring-like structure with the western core having very broad line widths. The line broadening of $\sim$3.5 km s^{-1} is also seen in the PV-plot made across the western core at PA = 15° (Fig. 6b). Additionally, we performed a third cut at PA = 140° (Fig. 6c), picking up the eastern side of the cavity and the eastern core. From this plot, it seems that there are two structures, a velocity gradient associated with the eastern core of $\sim$1.5 km s^{-1}

in a region of 7″ and a curve structure associated with the cavity. The curve structure seen in the PV-plot of Fig. 6c suggests that the cavity is expanding. Overall it seems that both cuts, at PA = 90° and PA = 140°, reveal expanding motions, suggesting that these motions could be produced by a combination of stellar winds, radiation, and/or molecular outflows from the central cluster. As a result, the AFGL 5142 cluster seems to be in process of disrupting the natal cloud. However, we will not discuss the kinematics of the region further since it is not the aim of this paper.

4. Analysis

4.1. Column density maps

We studied the chemical environment of AFGL 5142 by analyzing the column density of several molecular species. We used the N_2H^+ (1–0) (this work), NH_3 (1, 1) and NH_3 (2,2) from Zhang et al. (2002), and HCO^+ (1–0) and $H^{13}CO^+$ (1–0) from Hunter et al. (1999) data. To properly compare the emission of all the molecules, we convolved the N_2H^+, NH_3, HCO^+, and $H^{13}CO^+$ channel maps to obtain a final circular beam of $\sim$4″. We computed the column density maps by extracting the spectra for positions in a grid of 1″×1″. Using CLASS we fitted the hyperfine structure of each spectrum for N_2H^+ (1–0) and NH_3 (1, 1), and a single Gaussian for the NH_3 (2, 2), HCO^+ (1–0) and $H^{13}CO^+$ (1–0). We fitted only those positions with an intensity greater than 5σ for N_2H^+ (1–0) and NH_3 (1, 1) in order to ensure we are detecting all the hyperfine components, whereas for the other molecular species we fitted the spectra with an intensity greater than 4σ. In the following sections we show the method used to compute the column density for each molecule. The main results are summarized in Table 2.

4.1.1. N_2H^+

We used the hyperfine structure fitting program in CLASS (Forveille et al. 1989) adopting the hyperfine frequencies given in Caselli et al. (1995) to determine the v_{LSR}, the intrinsic line widths, total optical depths, and excitation temperatures (T_{ex}) in each position of the grid. The value of T_{ex} was derived assuming a filling factor of 1. As shown in Table 1, the excitation temperature, T_{ex}, derived from the hyperfine fits in the eastern core is in the range $\sim$14–16 K, while T_{ex} has lower values around $\sim$10– 12 K and $\sim$8–9 K for the western and central cores, respectively.

The results obtained from the fits indicate that the N_2H^+ emission is essentially optically thin for most of the region ($\tau_{TOT} \simeq$ 0.3–0.6); however, the optical depth in the western core reaches higher values, around $\tau_{TOT} \simeq$ 1.5–2. We calculated the N_2H^+ column density, corrected for the primary beam response, following the expression given in Caselli et al. (2002b),
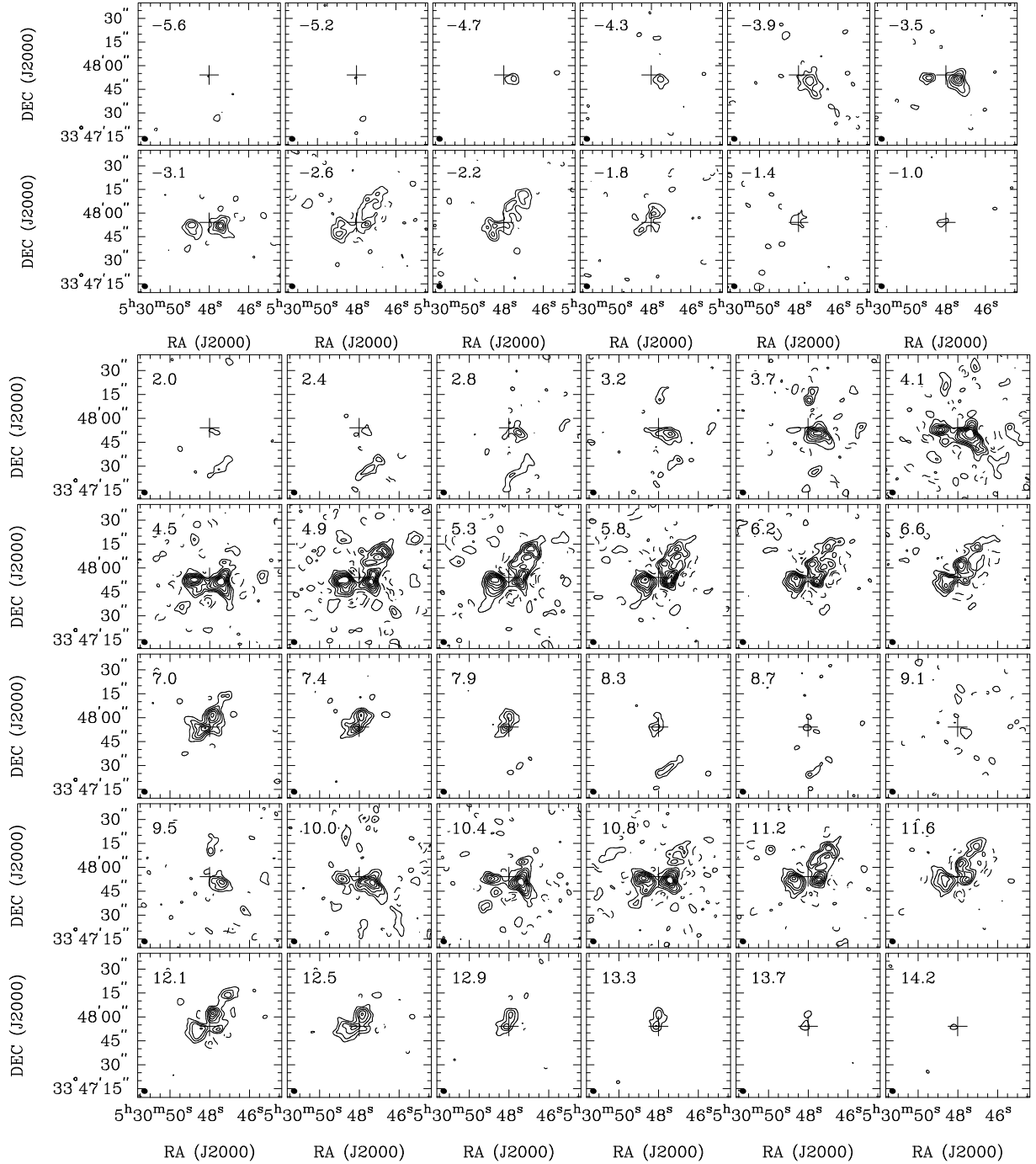
Fig. 3. *Top panel*: N$_2$H$^+$ (1–0) channel maps for the hyperfine $F_1F = 01 \rightarrow 12$ (isolated line) toward AFGL 5142. Contour levels are -2, 2, 4, 6, 8, 10, and 12 times the rms noise of the maps, 0.055 Jy beam^{-1}. *Bottom panel*: N$_2$H$^+$ (1–0) channel maps for the hyperfine $F_1F = 21 \rightarrow 11$, $23 \rightarrow 12$, $22 \rightarrow 11$, and $F_1F = 11 \rightarrow 10$, $12 \rightarrow 12$, and $10 \rightarrow 11$. Contour levels are -4, -2, 2, 4, 6, 8, 10, 12, and 14 times the rms of the map, 0.055 Jy beam^{-1}. In all panels the cross marks the position of the 3.2 mm continuum source. The synthesized beam is shown in the bottom left corner. Velocities referres to the $F_1F = 01 \rightarrow 12$ hyperfine with the systemic velocity $v_{\rm LSR} = -3$ km s^{-1}.

and approximating the partition function to $Q_{\rm rot} \simeq (kT_{\rm ex}/hB) \sim 0.4473\,T_{\rm ex}$, where k is the Boltzmann constant, $T_{\rm ex}$ the excitation temperature, h the Planck constant, and B the rotational constant of N$_2$H$^+$.

Figure 7a shows the resulting N$_2$H$^+$ column density map. Clearly, we found important variation in the N$_2$H$^+$ column density in AFGL 5142. The highest value of the N$_2$H$^+$ column density, 3×10^{13} cm^{-2}, is reached in the western core. Toward the eastern core we found values of the N$_2$H$^+$ column density around $\sim 1 \times 10^{13}$ cm^{-2}, while the N$_2$H$^+$ column density has

the lowest values, around ~ 1–5×10^{12} cm^{-2}, toward the millimeter condensation, i.e., toward the central core (see Table 2). The values found in the western and eastern cores are in good agreement with the N$_2$H$^+$ column densities reported by Pirogov et al. (2003, 2007) for dense molecular cloud cores with massive stars and star clusters and Fontani et al. (2006) for a sample of high-mass protostellar candidates. In addition, the values of the N$_2$H$^+$ column density found in the western and eastern cores of AFGL 5142 are also consistent with those reported in recent studies conducted toward massive star-forming regions observed
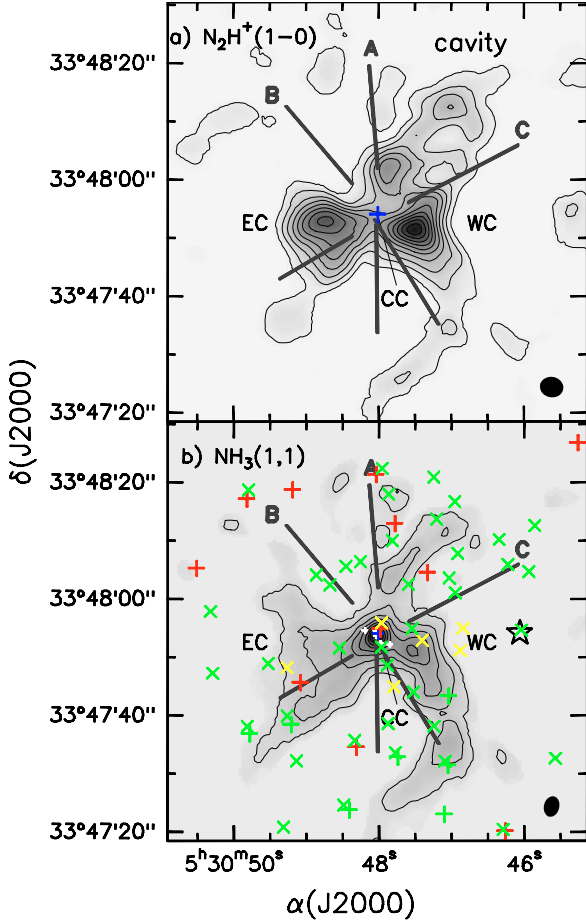
Fig. 4. a) N$_2$H$^+$ zero-order moment integrated for all the hyperfine components of the (1–0) transition. Contours start at 3%, increasing in steps of 10% of the peak intensity, 6.01 Jy beam^{-1}km s^{-1}. **b)** NH$_3$ (1, 1) zero-order moment (Zhang et al. 2002). Contours start at 10%, increasing in steps of 10% of the peak intensity, 0.202 Jy beam^{-1}km s^{-1}. The synthesized beams, 4″.04×3″.53 for N$_2$H$^+$ and 3″.58×2″.64 for NH$_3$, are shown in the bottom right corner. In both panels the blue cross marks the position of the millimeter source reported in this work. Red crosses: type I (protostars); green crosses: type II (class II objects) from Qiu et al. (2008). Yellow and green tilted crosses are from Chen et al. (2005) and represent Class I luminous protostars with $M < 5\,M_\odot$ and Herbig Ae/Be stars or T Tauri stars, respectively. White crosses are the 5 mm peaks detected with the SMA by Zhang et al. (2007), and the star marks the position of the IRAS 05274+3345. The western, eastern, and central cores are also labeled as WC, EC, and CC, respectively. The thick straight black lines represent the direction of outflows A, B, and C (Zhang et al. 2007).

with interferometers (e.g., Palau et al. 2007; Beuther & Henning 2009), but those obtained in the central core are clearly below. It is important to emphasize the difference of 1 order of magnitude in the N$_2$H$^+$ column density in the central core compared to the western and eastern cores. The uncertainty in the N$_2$H$^+$ column density lies between 25 and 50%, and it has been estimated taking into account the uncertainty in the output parameters of CLASS and the uncertainty in the calibration.

4.1.2. NH$_3$

The optical depth of the main line derived from the NH$_3$ emission is in the range $\tau_{\rm TOT} \simeq 1.5$–2.5 toward the central and compact NH$_3$ core containing the intermediate/high-mass stars, while the emission in the extended structure is optically thin.
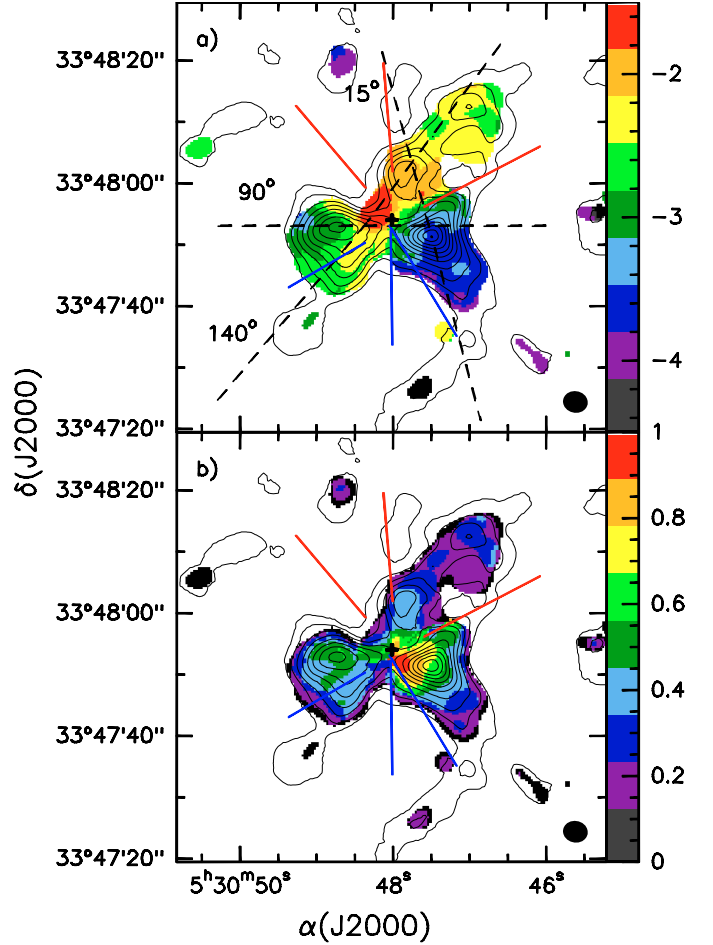
Fig. 5. a) First-order moment map (velocity) for the hyperfine $F_1F = 01 \rightarrow 12$ line of N$_2$H$^+$ (1–0) toward AFGL 5142 (color scale); **b)** second-order moment map (velocity dispersion) for the hyperfine $F_1F = 01 \rightarrow 12$ line of N$_2$H$^+$ (1-0) (color scale). In both figures, black contours are the same as in Fig. 4a, showing the N$_2$H$^+$ (1–0) emission, with contours starting at 3%, and increasing in steps of 10% of the peak intensity. Color scales are in km s^{-1}. The synthesized beam is shown in the bottom right corner of the image. The black cross marks the position of the 3.2 mm source reported in this work. Blue and red lines represent the direction of outflows A, B, and C (Zhang et al. 2007), and the black dashed line in the top panel indicates the position-velocity cuts (see Fig. 6). The second-order moment gives the velocity dispersion and must be multiplied by the factor $2\sqrt{2\ln 2} \simeq 2.35$ to convert to *FWHM*.

From the results of the fits of the NH$_3$ (1, 1) and NH$_3$ (2, 2) spectra, we derived the rotational temperature ($T_{\rm rot}$) and computed the NH$_3$ column density map following the procedures described in Ho & Townes (1983) and Harju et al. (1993) (see also the appendix of Busquet et al. 2009 for a description of the method). It is worth noting that the rotational temperature map obtained from this analysis is similar to the NH$_3$ (2, 2)/NH$_3$ (1, 1) intensity map presented in Zhang et al. (2002).

The NH$_3$ column density map, corrected for the primary beam attenuation, is shown in Fig. 7b. The map shows small variations along the entire cloud. In contrast to N$_2$H$^+$, the NH$_3$ column density reaches the maximum value, around 3×10^{15} cm^{-2}, toward the central core at the position of the millimeter condensation, and where we found the minimum N$_2$H$^+$ column density (see Table 2). The values found for the NH$_3$ column density toward AFGL 5142 are similar to those obtained by Palau et al. (2007) in the massive star-forming region IRAS 20293+3952.
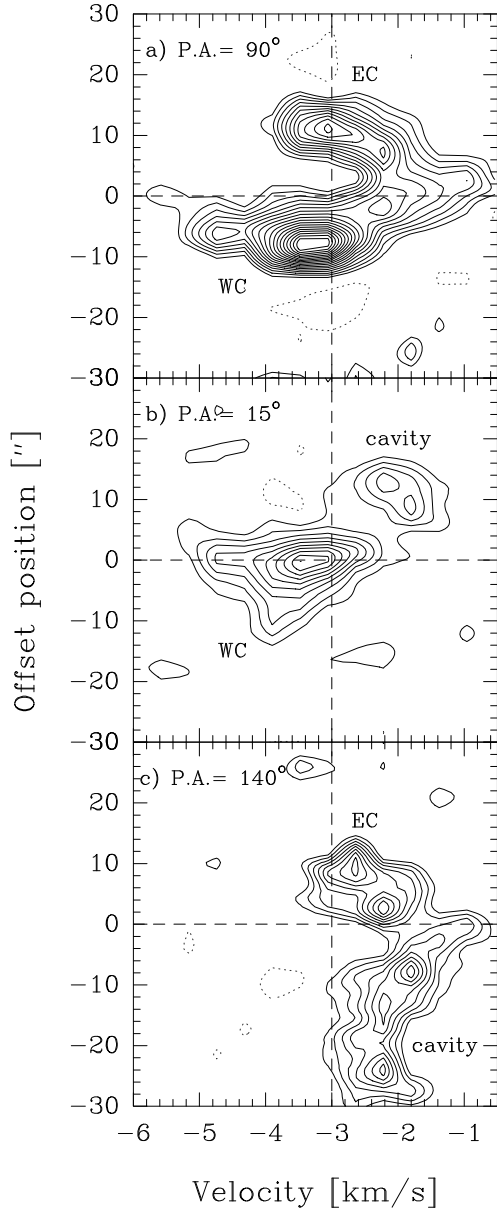
Fig. 6. N₂H⁺ $p-v$ plot for the $F_1 F = 01 \rightarrow 12$ hyperfine at **a)** PA = 90° (along the eastern and western cores). Channel maps have been convolved with a beam 6″×2″ with PA perpendicular to the direction of the cut. Contours start at 10%, increasing in steps of 5% of the peak emission, 0.408 Jy beam⁻¹. The central position corresponds to the 3.2 mm source. Positive offsets are toward the east; **b)** PA = 15°. Channel maps have been convolved with a beam 2″ × 2″. Contours start at 10%, increasing in steps of 10% of the peak emission, 0.601 Jy beam⁻¹. The central position is taken at the peak position of the western core, which is $\Delta x = -6.5$″, $\Delta y = -3$″ offset from the phase center. Positive offsets are toward the northeast. **c)** PA= 140°. Contours start at 20%, and increase in steps of 10% of the peak emission, 0.376 Jy beam⁻¹. Positive offsets are toward the southeast. The central position corresponds to $\Delta x = 3.9$″, $\Delta y = -0.59$″ offset from the phase center. In all panels, the vertical dashed line indicates the systemic velocity, $v_{LSR} = -3$ km s⁻¹.

The uncertainty in the NH₃ column density is ∼15–25%, estimated from the uncertainty in the rotational temperature (see Busquet et al. 2009), the output parameters of CLASS, and the uncertainty in the calibration.
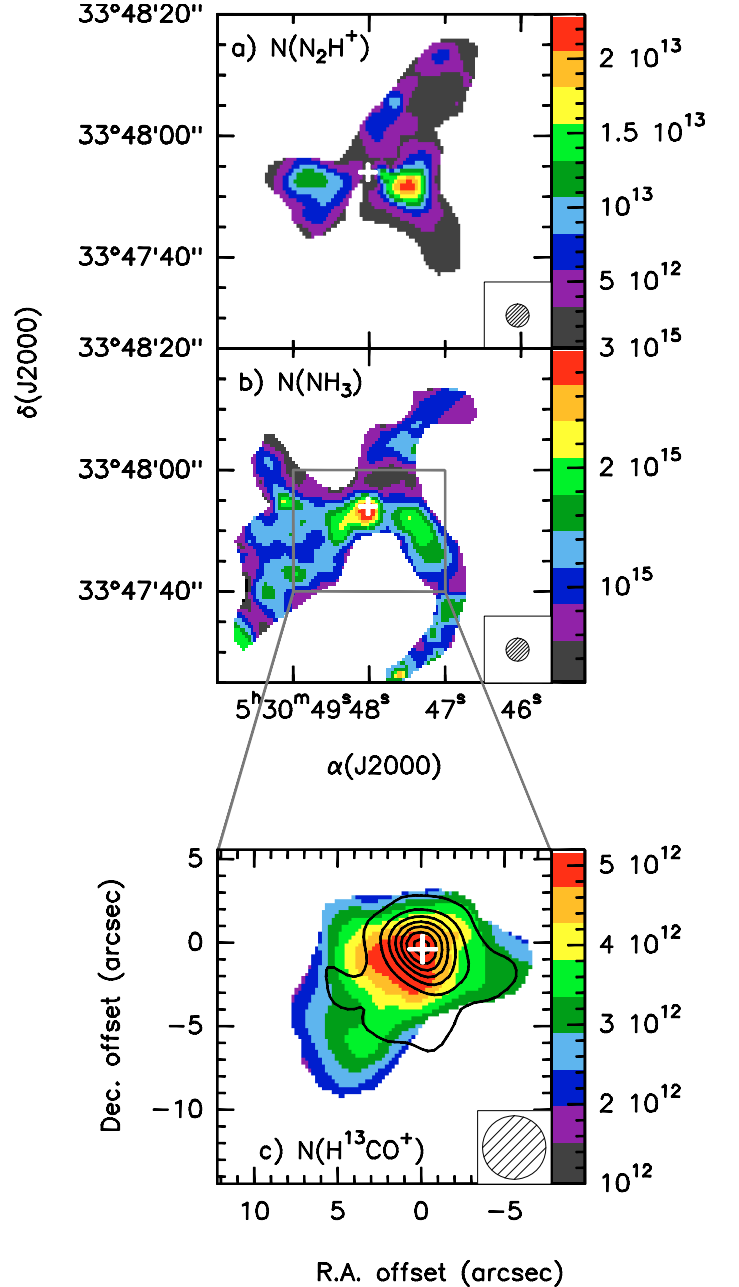

Fig. 7. **a)** N₂H⁺ column density map. **b)** NH₃ column density map. **c)** H¹³CO⁺ column density map overlaid with the 3.2 mm continuum emission (contours). In all panels scale units are cm⁻². The synthesized beam, ∼4″, is shown in the bottom right corner of each panel. The white cross marks the position of the 3.2 mm peak.

4.1.3. H¹³CO⁺

To derive the H¹³CO⁺ column density, we assumed that H¹³CO⁺ (1–0) emission is optically thin while HCO⁺ (1–0) is optically thick. The H¹³CO⁺ (1–0) optical depth has been estimated from the ratio of the H¹³CO⁺ and HCO⁺ integrated intensity emission obtained from Gaussian fits and excluding the high-velocity components of HCO⁺ (1–0) coming from molecular outflow emission.

Assuming that all levels are populated according to the same excitation temperature T_{ex} and approximating the partition function to kT_{ex}/hB, with B the rotational constant of the molecule,

Table 2. Average column density for each dense core.

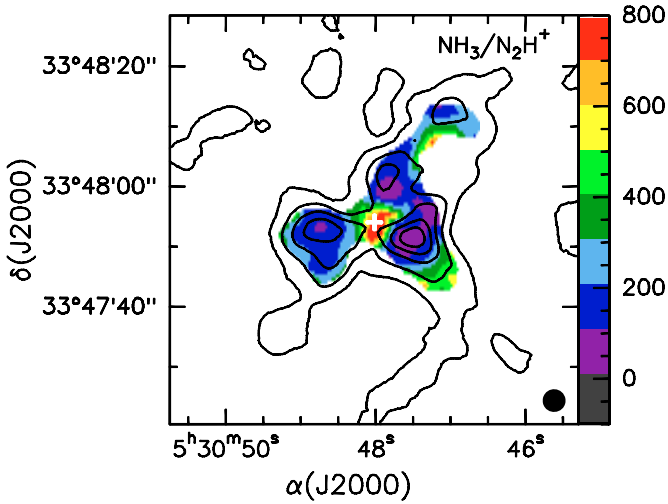| Core	$N(NH_3)$ (cm^{-2})	$N(N_2H^+)$ (cm^{-2})	$N(H^{13}CO^+)$ (cm^{-2})	$N(NH_3)/N(N_2H^+)$
central	2.6×10^{15}	2.5×10^{12}	4.5×10^{12}	1000
eastern	1.4×10^{15}	1.1×10^{13}	...	130
western	1.8×10^{15}	1.8×10^{13}	...	100

Fig. 8. Color scale: N(NH$_3$)/N(N$_2$H$^+$) abundance ratio map overlaid with the N$_2$H$^+$ emission (black contour), with contours starting at 3%, and increasing in steps of 20% of the peak intensity. The synthesized beam, ∼4″, is shown in the bottom right corner. The white cross marks the position of the 3.2 mm peak.

the column density of a linear molecule obtained from the transition $J \rightarrow J-1$ is

$$N = \frac{3k}{4\pi^3} \frac{1}{\mu^2 \nu_{10} J} T_{ex} \frac{\exp\left(\frac{J(J+1)}{2} \frac{h\nu_{10}}{kT_{ex}}\right)}{\exp\left(\frac{J}{} \frac{h\nu_{10}}{kT_{ex}}\right) - 1} \tau_0 \Delta v, \quad (1)$$

where μ is the electric dipole momentum of the molecule, ν_{10} the frequency of the transition $J = 1 \rightarrow 0$, and τ_0 the opacity at the line center.

For the particular case of H^{13}CO$^+$ (1–0) molecular transition, $\mu = 3.88$ Debye= 3.88×10^{-18} (cgs), $\nu_{10} = 86.754$ GHz, the column density can be written, in practical units, as

$$\left[\frac{N(H^{13}CO^+)}{cm^{-2}}\right] = 2.56 \times 10^{11} \frac{1}{1 - e^{-4.16/T_{ex}}} \left[\frac{T_{ex}}{K}\right] \tau_0 \left[\frac{\Delta v}{km\,s^{-1}}\right]. \quad (2)$$

In Fig. 7c we present the H^{13}CO$^+$ column density map toward the central core of AFGL 5142. An obvious feature is that the H^{13}CO$^+$ column density map is correlated with the NH$_3$ column density map, reaching the maximum value, around 5×10^{12} cm^{-2} toward the millimeter condensation, but is anticorrelated with the N$_2$H$^+$ column density. The values obtained for the H^{13}CO$^+$ column density are similar to those found toward regions of high-mass star formation (e.g., Zinchenko et al 2009). Taking the uncertainty in the output parameters of CLASS and the uncertainty in the calibration into account, we estimated an uncertainty in the H^{13}CO$^+$ column density around ∼30–45%.

4.2. The NH$_3$/N$_2$H$^+$ abundance ratio map

Figure 8 shows the NH$_3$/N$_2$H$^+$ abundance ratio map toward AFGL 5142. First of all, it is important to point out that the

N$_2$H$^+$ spectra toward some positions of the central core have low signal-to-noise, so only a few positions with high enough signal-to-noise ratio were fitted properly, so hence the values obtained toward the central core, especially those toward the southwestern side of the millimeter condensation, are overestimated due to the interpolation process. A clear feature seen from the NH$_3$/N$_2$H$^+$ ratio map is that the highest values, ranging from ∼400 up to 1000, are reached close to the position of the central core (i.e., harboring a cluster of millimeter sources). We explicitly checked that such high values are real so not produced by the interpolation process. Toward the western core, which could contain a low-mass YSO, we found values of the NH$_3$/N$_2$H$^+$ ratio around 50–100, whereas in the eastern core, maybe containing a more evolved object, the NH$_3$/N$_2$H$^+$ ratio is around 50–100 toward the center of the core and increases up to 200 at the edges. In Table 2 we give the average value of the NH$_3$/N$_2$H$^+$ ratio for these three cores. The uncertainty estimated for the NH$_3$/N$_2$H$^+$ abundance ratio is around ∼30–60%. As already pointed out by Zhang et al. (2002), the VLA NH$_3$ data recover 65% of the flux observed by the Effelsberg 100 m telescope (Estalella et al. 1993), and the missing flux arises mainly from smooth structures with scales larger than 50″. Unfortunately, we cannot estimate the amount of flux filtered out by CARMA in N$_2$H$^+$ due to the lack of short-spacing information. However, since the CARMA N$_2$H$^+$ and VLA NH$_3$ images are sensitive to similar angular scales, the NH$_3$/N$_2$H$^+$ ratio is not seriously affected by differences in the missing flux.

5. Chemical modeling

5.1. The UCL_CHEM model

We employed UCL_CHEM, a time- and depth- dependent chemical model similar to the one used in Viti & Williams (1999) and Viti et al. (2001, 2004) to study the behavior of the NH$_3$/N$_2$H$^+$ abundance ratio. For simplicity, in this study we performed time-dependent single-point calculations. The model consists of a two-phase calculation. In phase I we follow the chemical and dynamical evolution of a collapsing core. This phase starts from a fairly diffuse medium ($n \simeq 400$ cm^{-3}) in neutral atomic form (apart from a fraction of hydrogen in H$_2$) that undergoes a collapse following the free-fall collapse law described in Rawlings et al. (1992) until densities typical of massive dense cores ($n \simeq 10^5 - 10^7$ cm^{-3}) are reached. During this time, atoms and molecules from the gas freeze on to the dust grains and hydrogenate where possible, as in Viti & Williams (1999). The degree of freeze out or depletion, defined in terms of the depletion of the CO molecule, is a free parameter (although linked with density, see Rawlings et al. 1992), which we explore in this study. During phase I we adopted a constant temperature of 12 K and assumed a standard value for the cosmic ionization rate, $\zeta = 3 \times 10^{-17}$ s^{-1}. The initial gas-phase elemental abundances relative to hydrogen nuclei adopted in this work, based on the findings of Sofia & Meyer (2001), are listed in Table 3. We included 127 gas-phase species and 42 surface species interacting in 1869 chemical reactions adapted from the UMIST 2006 database (Woodall et al. 2007). During the collapse phase (phase I), we let the chemistry develop for 3 Myr, regardless of when the final density is reached.

In phase II we explored the chemical evolution of the core that harbors a newly born massive star by simulating the presence of an infrared source at the center of the core and by subjecting the core to a time-dependent increase of the gas and dust temperature (assumed to be the same because of the high

Table 3. Initial gas-phase elemental abundances relative to hydrogen nuclei.

Atom	Abundance
H	1.0
He	0.075
O	4.45×10^{-4}
C	1.79×10^{-4}
N	8.52×10^{-5}
S	1.43×10^{-6}
Mg	5.12×10^{-6}

Table 4. Parameters of the UCL_CHEM model.

Parameter	CC[a]	WC and EC[b]
Depletion[c] (%)	99	99
Gas Density[c] (cm^{-3})	10^6	10^5
A_v[c]	41	10
T_{max}[d]	70	25

Notes. [a] CC: central core; [b] WC and EC: western and eastern cores; [c] at the end of phase I; [d] maximum value reached during phase II.

densities considered), which was performed differently depending on the core we were modeling. For the central core we adopted a maximum temperature of ~70 K, whereas the temperature toward the western and eastern cores is around ~25 K (both derived from NH$_3$ data, see Zhang et al. 2002). During phase II we performed the same treatment for the increasing temperature and evaporation from grains as in Viti et al. (2004), which includes the experimental results on desorption from grains and the evaporation of icy mantles formed in star-forming regions (Collings et al. 2003a,b, 2004). In this case, the evaporation of a fraction of mantle species occur when the temperature for a particular desorption event is reached (see Viti et al. 2004, for a complete description). In phase II we followed the evolution of each core for 3 Myr.

5.2. Results

We computed a grid of models to investigate the differences observed in the N$_2$H$^+$ column density and the NH$_3$/N$_2$H$^+$ abundance ratio. For the central core we followed the chemical evolution of a core of 0.02 pc in diameter, whereas we adopted a size of 0.04 pc for the eastern and western cores. We explored a range of densities, $n \simeq 10^5$–10^7 cm^{-3}, and for a particular density we used different percentages of freeze-out at the end of phase I. From this analysis we found that the observed values of the NH$_3$/N$_2$H$^+$ ratio can be reproduced by our model using a high degree of depletion at the end of the collapse phase (phase I) and by adopting a density $n \simeq 10^6$ cm^{-3} for the central core and $n \simeq 10^5$ cm^{-3} for the western/eastern cores. It is worth noting that the model for the central core is supported by our estimate of the density from the dust continuum emission. Adopting the mass derived in this work (see Sect. 3.1) and a size of 6″, we obtained a density of ~5×10^6 cm^{-3}, consistent with the density adopted in the chemical model. In Table 4 we list the parameter choices for the two selected models (CC and WC/EC models), which can reproduce both the observed NH$_3$ and N$_2$H$^+$ column densities and the NH$_3$/N$_2$H$^+$ abundance ratio. In the following sections, we discuss the main results obtained by our chemical model for phases I and II.

5.2.1. Fractional abundances and the NH$_3$/N$_2$H$^+$ abundance ratio during phase I

In Fig. 9 (left panels) we present the fractional abundances (with respect to hydrogen nuclei) of some molecular species of interest (i.e., CO, N$_2$, H$_3^+$, NH$_3$, N$_2$H$^+$, and HCO$^+$), together with the NH$_3$/N$_2$H$^+$ abundance ratio as a function of time for the central core (CC model) and the western/eastern cores (WC/EC model) during phase I. First of all, the fractional abundances obtained for the central core (top panel) and the western/eastern cores (middle panel) do not show significant differences because they only differ in the core size and the final density reached at the end of this phase. As can be seen in Fig. 9, the fractional abundance of CO, N$_2$, NH$_3$, N$_2$H$^+$, and HCO$^+$ increases with time (with a more pronounced increase for the case of CO, N$_2$, and NH$_3$), reaching its maximum value at times $t \simeq 2.5 \times 10^6$ yr. After this time, the fractional abundances start to decrease because molecules freeze out onto dust grains due to the low temperature ($T \simeq 12$ K) and high density ($n \simeq 10^5$–10^6 cm^{-3}) achieved in these cores. On the other hand, the ion H$_3^+$ keeps more or less a constant abundance until $t \simeq 2.5 \times 10^6$ yr, and then its abundance rises moderately.

The primary formation route for N$_2$H$^+$ is through the reaction between H and N$_2$, which also produces H$_2$. N$_2$H$^+$ can then react with many atoms and molecules such as C, O, H$_2$O, or CO to form N$_2$. It is therefore clear that the abundance in the gas phase of these removal agents will be critical in determining the abundance of N$_2$H$^+$ present. At high densitites, but before the effects of freeze-out dominate, all the molecular species that are important in the removal of N$_2$H$^+$ and NH$_3$ will be high. In particular, for both models the main formation route for N$_2$H$^+$ is initially H$_2$ + N$_2^+$ $\rightarrow$ N$_2$H$^+$ + H, and then the chemical reaction H$_3^+$ + N$_2$ $\rightarrow$ N$_2$H$^+$ + H becomes important, while NH$_3$ is mainly formed via dissociative recombination of NH$_4^+$. The latter is formed via consecutive hydrogenation of N$^+$ (via reactions with molecular hydrogen).

During phase I the NH$_3$/N$_2$H$^+$ abundance ratio behaves in the same way for both the central core and the western/eastern cores models, and only during the latest time steps does it depend on the adopted density ($n \simeq 10^5$ cm^{-3} for the western/eastern cores and $n \simeq 10^6$ cm^{-3} for the central core). In both cases, the NH$_3$/N$_2$H$^+$ ratio starts from low values and reaches values around 1000 and even higher for $t > 2.5 \times 10^6$ yr because CO depletion favors the formation of NH$_3$ against N$_2$H$^+$ in core centers at high densities. This suggests that long-lived starless cores are associated with high values of the NH$_3$/N$_2$H$^+$ abundance ratio.

5.2.2. Fractional abundances and the NH$_3$/N$_2$H$^+$ abundance ratio during phase II

Figure 9 (right panels) shows the fractional abundances (with respect to hydrogen nuclei) as a function of time of CO, N$_2$, H$_3^+$, NH$_3$, N$_2$H$^+$, and HCO$^+$ derived from our chemical model during phase II for the central core (top panel) and the western/eastern cores (middle panel). The fractional abundances in the central core clearly have a different behavior compared to that of the western and eastern cores as a consequence of the different density, and especially the different temperature reached at the end of phase II. In the central core, the fractional abundance of CO, N$_2$, N$_2$H$^+$, and HCO$^+$ is constant during the initial stages, and once the temperature increases, their fractional abundances rise significantly. On the other hand, the fractional abundance of the molecular ion H$_3^+$ decreases with time. This is of course because
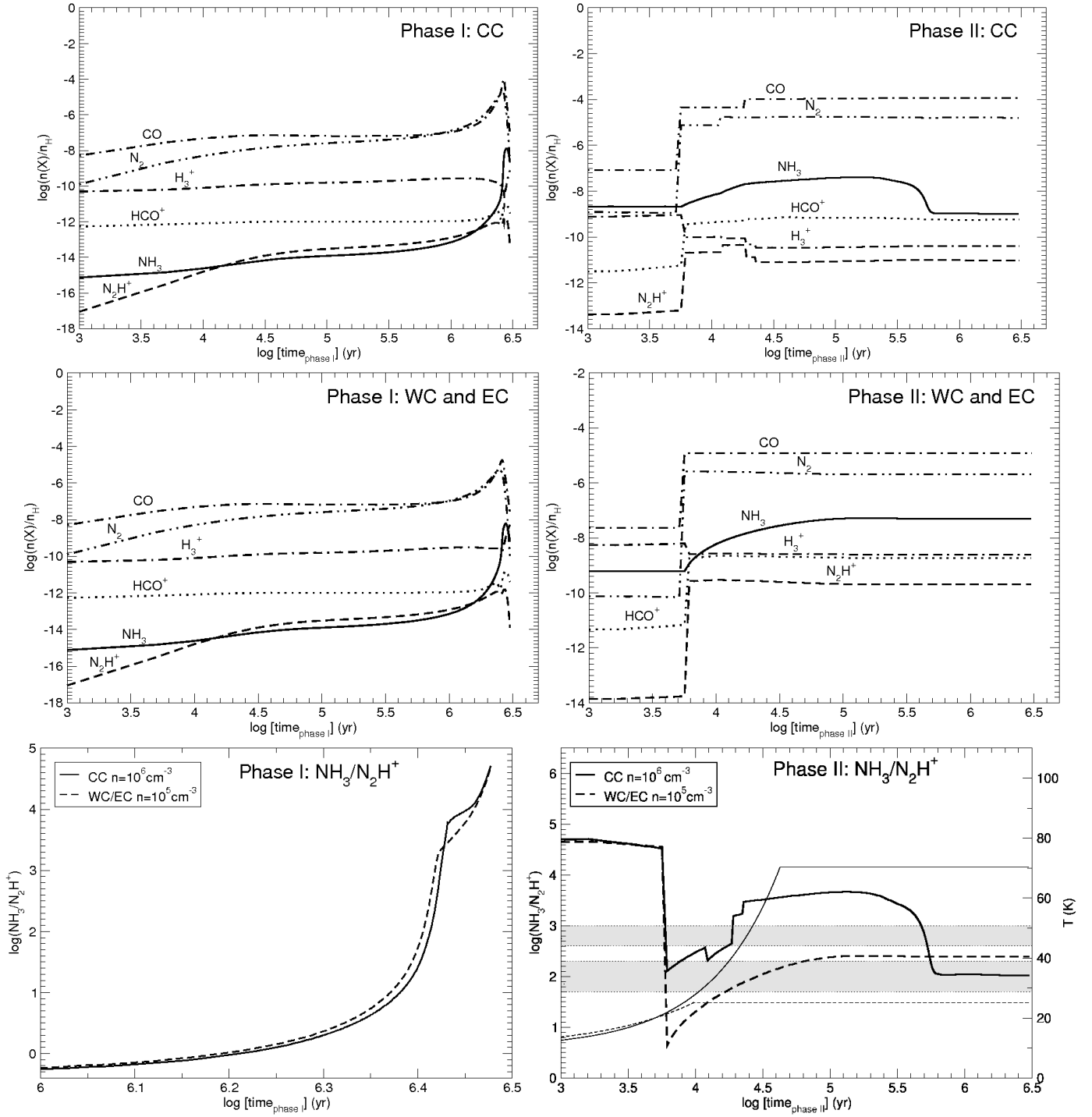
Fig. 9. *Left*: fractional abundances with respect to hydrogen as a function of time during phase I for the central core (*top panel*) and the western/eastern cores (*middle panel*). The NH_3/N_2H^+ abundance ratio for both the central core and the western/eastern core are also shown in the *bottom panel*. *Right*: same as left panels but for phase II calculation. The y-axis ranges according to the model. In the bottom right panel we also show the temperature as a function of time, indicated by the thin lines. The two shaded areas mark the range of values (400–1000 for the central core and 50–200 for the western/eastern cores) of the NH_3/N_2H^+ abundance ratio estimated from the observational data.

Table 5. Results obtained from the chemical model.

Model	Time (yr)	$N(NH_3)$ ($\times 10^{14}$ cm^{-2})	$N(N_2H^+)$ ($\times 10^{11}$ cm^{-2})	NH_3/N_2H^+
CC	1.9×10^4	17	38	450
CC	4.5×10^5–5.3×10^5	11–3.20	0.80	1400–400
WC & EC	1×10^4–3×10^6	2.80–10	56–41	50–240

H_3^+ is highly reactive at high densities. The abrupt increase in the fractional abundance takes place at the same time for all molecules, around $t \simeq 6.1 \times 10^3$ yr (corresponding to a temperature of $T \simeq 21$ K). This time corresponds to the time when a fraction of weakly bound species evaporates from the grain mantle (see Table 1 in Viti et al. 2004). The fractional abundance of N_2H^+ reaches its maximum value 4.6×10^{-11} (corresponding to a N_2H^+ column density of $\sim 1.8 \times 10^{12}$ cm^{-2}) at $t \simeq 1.7 \times 10^4$ yr. The rapid destruction of N_2H^+ (by the chemical reaction $N_2H^+ + CO \rightarrow HCO^+ + N_2$) occurs at $t \simeq 2.3 \times 10^4$ yr, with a variation in the fractional abundance of one oder of magnitude, with the N_2H^+ column density around $\sim 8 \times 10^{11}$ cm^{-2}, consistent with the value estimated from the observations. On the other hand, HCO^+ fractional abundance is constant at $\sim 6 \times 10^{-10}$. Assuming $[HCO^+/H^{13}CO^+] = 40$, we estimated an $H^{13}CO^+$ column density of $\sim 1.3 \times 10^{12}$ cm^{-2}, in good agreement with the estimation from the observational data (see Table 2). This chemical behavior could be explained in terms of CO desorption from grain mantles, which causes a substantial destruction of N_2H^+ favoring the formation of HCO^+, where this reaction is the main removal mechanism of N_2H^+ for "standard" CO abundances of $[CO/H_2] \simeq 10^{-4}$ (Jørgensen et al. 2004b; Lee et al. 2004). In fact, as can be seen in Fig. 9 (top panel), the CO fractional abundance is $\sim 10^{-4}$, high enough to lead to significant destruction of N_2H^+.

In contrast to the case of N_2H^+ and HCO^+, the increase in the NH_3 fractional abundance is slow, which indicates that gas phase chemistry dominates pure evaporation. This is simply a consequence of most of the ammonia being still locked in water ice; in fact, as shown by the experiments by Collings et al. (2004), ammonia is released back into the gas phase only if temperatures of ~ 100–120 K are reached (Viti et al. 2004). The maximum value, of 4.1×10^{-8} (or $N(NH_3) \simeq 3.2 \times 10^{15}$ cm^{-2}), is reached at $t \simeq 1.3 \times 10^5$ yr, and then it drops until it reaches a constant abundance of 1×10^{-9} (or a column density of $\sim 8.2 \times 10^{13}$ cm^{-2}). This behavior, i.e., the decrease in the NH_3 fractional abundance, takes place through reactions of the NH_3 molecule with the ions C^+ and HCO^+. In this situation, the C^+ fractional abundance increases at late stages, while the fractional abundance of HCO^+ is more or less constant, which is consistent with HCO^+ being produced from the destruction of N_2H^+ (see above) and destroyed through reactions with NH_3.

Regarding the western and eastern cores, which were modeled assuming the same core size (~ 0.04 pc) and same temperature (the maximum temperature is 25 K), we found that the fractional abundance of NH_3 increases moderately with time, while the fractional abundances of CO, N_2, N_2H^+, and HCO^+ rise considerably during the initial stages due to desorption effects, similar to the case of the the central core model. At $t \simeq 4 \times 10^3$ yr, N_2H^+ and HCO^+ have constant abundance, around $\sim 2 \times 10^{-10}$ ($N(N_2H^+) \simeq 4 \times 10^{12}$ cm^{-2}) and $\sim 1.8 \times 10^{-9}$ ($N(HCO^+) \simeq 3.6 \times 10^{13}$ cm^{-2} or $N(H^{13}CO^+) = 9 \times 10^{11}$ cm^{-2}, assuming $[HCO^+/H^{13}CO^+] = 40$) for N_2H^+ and HCO^+, respectively, while the NH_3 fractional abundance increases, up to $\sim 5.2 \times 10^{-8}$ ($N(NH_3) \simeq 1 \times 10^{15}$ cm^{-2}) at $t \simeq 1.3 \times 10^5$ yr, and then remains roughly constant, too. For these cores, the values obtained from the chemical modeling agree (within a factor of 2 in the case of N_2H^+, and a factor of 4 in the case of NH_3) with the column densities reported from the observational data. Finally, the CO fractional abundance in the western/eastern cores is $\sim 10^{-5}$, significantly lower than the CO fractional abundance of the central core, indicating that the relatively low CO abundance in the western/eastern cores does not lead to a substantial destruction of N_2H^+. Therefore, the fraction of CO that will evaporate from grain mantles plays an important role in determining the fractional abundance of N_2H^+, hence the NH_3/N_2H^+ abundance ratio.

In Table 5 we show the values of the NH_3 and N_2H^+ column densities, together with the NH_3/N_2H^+ abundance ratio for the two models that agree with the observed values. In Fig. 9 (bottom right panel) we present the NH_3/N_2H^+ abundance ratio as a function of time for the central core and the western/eastern core obtained during phase II. The NH_3/N_2H^+ abundance ratio observed toward the central core, around ~ 400–1000, can be reproduced by our chemical model for times $t \simeq 10^4$ yr and $t = (4.5$–$5.3) \times 10^5$ yr. For the time range $t \simeq 10^4$–4.5×10^5 yr, the model produces a higher NH_3/N_2H^+ abundance ratio, ~ 4000, slightly above the observed values for the central core. However, we adopted the longer age as it is more realistic. For the western/eastern cores, the NH_3/N_2H^+ abundance ratio initially shows high values, then it decreases due to desorption effects and finally reaches a constant value ~ 200 for typical ages of low-mass YSOs, at around $t \simeq 10^5$–10^6 yr. In addition, in Fig. 9 (bottom panel) we also show the temperature as a function of time. For the central core, when the temperature is low, the NH_3/N_2H^+ ratio is high ($>10^4$). Around $T \simeq 21$ K there is a clear drop in the NH_3/N_2H^+ ratio due to desorption effects. As temperature increases, the NH_3/N_2H^+ rises until it reaches a constant value, $\sim 10^3$, at around $T \simeq 45$ K. For the western and eastern cores the temperature varies from 12 to 25 K, producing small variations in the NH_3/N_2H^+ ratio, and only for times in the range 10^3–10^4 yr does the NH_3/N_2H^+ ratio change significantly, similar to the case of the central core. It is worth noting that in the model for the central core, the visual extinction is $A_V \simeq 40$, but typically the visual extinction in hot cores (i.e., embedded in the central core) is around ~ 100 or even higher. To evaluate the error in the NH_3/N_2H^+ abundance introduced by this difference, we performed an additional model with a higher density, which gives a visual extinction of $A_v \simeq 100$. In this situation, the NH_3/N_2H^+ ratio is affected by a difference of ~ 3–25%. The abrupt drop in the NH_3/N_2H^+ ratio produced at early ages ($t \simeq 5 \times 10^3$ yr) in both the central core and western/eastern cores stems from to desorption effects of some molecules.

Finally, we explored the fractional abundances of other molecular species and compared them with observations when available or made some predictions for future observations. We found that the fractional abundance of CH_3CN obtained from the chemical model is in the range $\sim 8 \times 10^{-8}$–10^{-7} at $t = (4.5$–$5.5) \times 10^5$ yr, in agreement with the value reported by Zhang et al. (2007), which is in the range $(1$–$4) \times 10^{-8}$. Additionally, our model predicts a CO abundance of 10^{-4} indicating that CO is desorbed from grain mantles due to the relatively high temperature (around ~ 70 K) and the powerful molecular outflows detected in CO (Zhang et al. 2007). We found that molecules like HC_3N, H_2CO, C_2H, and CS should be detectable toward the central core, since their fractional abundances are even higher than the NH_3 ones. Concerning the western and eastern cores, the CO fractional abundance, of 10^{-5}, is one order of magnitude lower than that of the central core. For these cores, molecules such as CS, C_2H, and CH_3CN are quite abundant and would be detectable, but we would not expect to detect any H_2CO and HC_3N.

In summary, the models that can reproduce the observed values of the NH_3/N_2H^+ abundance ratio toward the central core, as well as in the western and eastern cores, were obtained with a high depletion at the end of phase I. The differences between the central and the western/eastern cores seen in the NH_3/N_2H^+ abundance ratio therefore seem to mainly come from density and

temperature effects. In particular, as shown by the chemical modeling of the region, the temperature is a key parameter in determining the NH_3/N_2H^+ abundance ratio, hence the abundance of each molecule. As temperature rises, the fraction of species that will evaporate increases, and consequently the chemistry evolves differently.

6. Discussion

The results obtained from the N_2H^+ observations, together with NH_3 data from the literature (Zhang et al. 2002) show that there are three dense cores associated with the high-mass star-forming region AFGL 5142. The central core, strong in NH_3 but almost devoid of N_2H^+, harbors a cluster of massive stars in their making. On the other hand, the western and eastern cores are stronger in N_2H^+ than in NH_3 emission. In the following section, we discuss the possible reasons for the observed variation in the NH_3 / N_2H^+ abundance ratio among the cores found in AFGL 5142.

The central dense core in AFGL 5142 is actively forming a cluster of massive stars, still in the accretion phase, which displays the typical signposts of star formation (molecular outflow and maser emission). Concerning the western and eastern cores, the relatively high temperature, around 20 K, could be due to the presence of an embedded YSO and/or heating produced by the three molecular outflows associated with the central core, which strongly affects the surrounding dense gas (Zhang et al. 2002, 2007). Thus, the association of the western and eastern cores with an infrared source is not obvious.

The NH_3/N_2H^+ abundance ratio map presented in Fig. 8 shows significant variations with a ratio around ~50–100 toward the western and eastern cores and a ratio up to 1000 toward the central core, due to a significant drop in the N_2H^+ abundance. The values found for the NH_3/N_2H^+ abundance ratio in the western and eastern cores are similar to those found in previous studies for cores harboring YSOs, for both low- and high-mass star-forming regions (Caselli et al. 2002a; Hotzel et al. 2004; Palau et al. 2007; Friesen et al. 2010). These studies are all consistent with a high ratio (≤ 300) that seems to be associated with starless cores, and a low ratio around 60–90 is found toward the YSOs, suggesting an anticorrelation between the the NH_3/N_2H^+ abundance ratio and the evolutionary stage. Thus, the high NH_3/N_2H^+ ratio toward the central core does not follow the anticorrelation between the NH_3/N_2H^+ ratio and the evolutionary stage of the core as in the studies mentioned above. The noticeable increase in the NH_3/N_2H^+ ratio in the central core suggests a strong differentiation of the N_2H^+ abundance between the central core and the western/eastern cores. Below we briefly investigate the origin of such a differentiation.

UV radiation effects:

As suggested by Qiu et al. (2008), UV photons from IRAS 05274+334 are not likely to affect the dense gas, and the effects of the UV field from the embedded protostar(s) do not seem to be a major concern in determining the NH_3 and N_2H^+ abundance of the central core, since the high visual extinction, $A_V \simeq 40$ mag or higher, prevents UV photons from penetrating the central core.

Excitation effects:

Even though we considered the effects of opacity and different T_{ex} in the calculation of the column densities, we consider whether the different excitation conditions among the dense cores may be the cause of the lower abundance of N_2H^+, i.e., the high NH_3/N_2H^+ ratio. The critical density of N_2H^+ is ~10^5 cm^{-3} (Jørgensen 2004a), while the critical density of NH_3 is ~10^4 cm^{-3} (Ho 1977). From the dust continuum emission, we estimated a density of ~10^6 cm^{-3} in the central core. In addition, the density obtained from single-dish observations at 850 μm (Jenness et al. 1995), adopting a core size of ~26″, is ~4×10^5 cm^{-3}. For these densities the transitions of both NH_3 and N_2H^+ are thermalized, and thus excitation effects do not seem appropriate to explain the N_2H^+ emission drop in the central core.

On the other hand, the hyperfine structure method in CLASS assumes equal excitation temperature for all the hyperfine components. Daniel et al. (2006) show that this assumption does not hold for the case of high opacities due to radiative processes. Since in AFGL 5142 we derived an opacity of $\tau_{TOT} \simeq 0.3$–0.6 for the N_2H^+ molecule, the problem reported by Daniel et al. (2006) is not likely to affect our result.

Physical and chemical effects:

The high values up to 1000 of the NH_3/N_2H^+ abundance ratio found in the central core of AFGL 5142 can be reproduced by our chemical model for high densities ($n \simeq 10^6$ cm^{-3}) and high temperaures ($T \simeq 70$ K). The chemical modeling performed in Sect. 5 indicates that both density and temperature play an important role in determining the molecular abundance of NH_3 and N_2H^+, hence their ratio. The central core has a higher temperature and density than the western and eastern cores. Thus, a different chemistry can develop due to CO evaporation from the grain mantles. The CO desorption in the central core of AFGL 5142 leads to the destruction of N_2H^+, so that the NH_3/N_2H^+ abundance ratio increases considerably relative to the value found in the western and eastern cores. This is supported by the fact that ^{13}CO is not frozen out in the central core, whereas it is faintly detected in the western and eastern cores (Zhang et al. 2007). As pointed out in Sect. 5.2.2, Collings et al. (2004) find experimental evidence that the desorption of NH_3 from grain mantles takes place at a temperature of ~120 K. Therefore, since in our model we assumed a maximum temperature of 70 K, the high NH_3/N_2H^+ abundance ratio in the central core is mainly a consequence of the destruction of N_2H^+ by CO rather than an enhancement of NH_3 in the gas phase. The disappearance of N_2H^+ from the gas phase has been reported by several authors, both in low- and high-mass star-forming regions. In the low-mass regime, there are several reports of central N_2H^+ depletion in Class 0/Class I protostars (e.g., IRAM 04191+1522: Belloche & André 2004; VLA 1623: Di Francesco et al. 2004; L483 mm: Jørgensen 2004a; Barnard 1c: Matthews et al. 2006; BHR 71 IRS1: Chen et al. 2008). Regarding the high-mass regime, Pirogov et al. (2003, 2007) used a single-dish telescope to observed a sample of dense cores associated with massive stars and star clusters containing IRAS point sources, and find that, for most of the sources, there is a decrease in the N_2H^+ abundance toward the dust column density peak. Furthermore, interferometric observations of N_2H^+ toward the high-mass star-forming regions IRAS 23033+5951 (Reid & Matthews 2008) also reveal a significant destruction of N_2H^+. Therefore, the high ratio measured toward the central core of AFGL 5142 seems to come from the rapid destruction of N_2H^+ when CO is released from grain mantles as seems to be the case for the other regions cited above.

Evolutionary effects:

Although in our chemical model we did not include molecular outflows, they may strongly affect the surrounding dense gas, hence the NH_3/N_2H^+ abundance ratio. As already discussed by Chen et al. (2008), who propose three stages in the interaction between the N_2H^+ emission and molecular outflows, based on the morphology of the N_2H^+ dense gas and the jet/outflow emission. Here we suggest a qualitative picture of the evolution of the NH_3/N_2H^+ abundance ratio. First, in starless cores with high densities, most molecules are highly depleted, which favors the formation of NH_3 and N_2H^+. It seems that the CO depletion favors the formation of NH_3 against N_2H^+ in core centers at high densities. Thus, the NH_3/N_2H^+ ratio reaches high values, consistent with the results found in low-mass starless cores (Caselli et al. 2002a; Hotzel et al. 2004; Friesen et al. 2010) as well as for starless cores nearby massive stars, like in the high-mass star-forming regions IRAS 20293+3952 (Palau et al. 2007). The high NH_3/N_2H^+ ratio in starless cores has been reproduced by our chemical model shown in Fig. 9 (left panels). After this phase, once the star has formed, the NH_3/N_2H^+ ratio decreases, as found in the low-mass regime (Caselli et al. 2002a; Hotzel et al. 2004; Friesen et al. 2010), and in YSOs close to the massive star (e.g., IRAS 20293+3952: Palau et al. 2007; IRAS 00117+612: Busquet et al. in prep.). In this situation, CO is less depleted, and N_2H^+ molecules in the envelope are entrained by the molecular outflow, with the N_2H^+ emission elongated in the direction of the molecular outflow, as found in IRAS 20293+3952 (Palau et al. 2007) and IRAS 00117+6412 (Palau et al. 2010). Finally, the next evolutionary stage involves the release of CO by powerful molecular outflows, which leads to the destruction of N_2H^+ and forms large holes in the envelope. Then, the NH_3/N_2H^+ abundance ratio raises considerably, like in the central core of AFGL 5142.

Therefore, either molecular outflows and density/temperature effects seem to be key pieces in the determination of the NH_3/N_2H^+ abundance ratio. To quantify the importance of the temperature in the NH_3/N_2H^+ ratio, we compared the results obtained in AFGl 5142 with the low-mass star-forming region L483. This region seems to be in the same stage of disruption of the envelope as AFGL5142, as the N_2H^+ shows two clumps on both sides of the YSO (see Jørgensen 2004a; Fuller & Wootten 2000), being then in the later evolutionary stage of the scenario proposed above. However, the NH_3 emission in L483 also shows a hole close to the position of the YSO, suggesting that possibly the NH_3/N_2H^+ abundance ratio is much lower than the values found in AFGL 5142, around 400–1000. This seems to indicate that the effects of molecular outflows alone cannot explain the high values derived in AFGL 5142, although this should be modeled to draw a firm conclusion. Thus, the high temperature reached in the central core due to the presence of hot cores seems to affect significantly the NH_3/N_2H^+ abundance ratio, indicating that the NH_3/N_2H^+ ratio behaves differently than in low-mass star-forming regions.

7. Conclusions

We used CARMA to observe the 3.2 mm continuum emission and the N_2H^+ molecular line emission toward the massive protostellar cluster AFGL 5142. The N_2H^+ dense gas emission, which mimics the morphology of NH_3, shows two main cores, one to the west (the western core) of the dust condensation of ~0.08 pc of size and another core to the east (the eastern core), of ~0.09 pc. Interestingly, toward the dust condensation,

of $M \simeq 23\,M_\odot$, the N_2H^+ emission drops significantly, whereas the compact NH_3 core (i.e., the central core) peaks at this position. The analysis of the N_2H^+ column density and the NH_3/N_2H^+ abundance ratio indicates a strong differentiation in the N_2H^+ abundance. While we found low values around ~50–100 of the NH_3/N_2H^+ abundance ratio associated with the western and eastern cores, the NH_3/N_2H^+ ratio rises significantly up to 1000 toward the central core, in which the formation of several massive stars is taking place. We performed a chemical modeling of the region using the time-dependent chemical model UCL_CHEM. The chemical model shows that a high NH_3/N_2H^+ abundance ratio can be reproduced in three different situations: i) in long-lived starless cores; ii) in high density cores with low temperature, ~20–25 K, and containing YSOs; and iii) in high density cores with YSOs and high temperature.

For the central core we found that such a high value of the NH_3/N_2H^+ abundance ratio could be explained with a density of ~10^6 cm^{-3} and a maximum temperature of 70 K, producing a substantial destruction of the N_2H^+ molecule by CO, which is desorbed from the grains mantles due to the high temperature and possibly the molecular outflows associated with the massive YSOs embedded in the central core. On the other hand, to reproduce the observed NH_3/N_2H^+ abundance ratio toward the western and eastern cores, we used a lower density of ~10^5 cm^{-3} and temperature (maximum temperature reached is 25 K). These results suggests that, in addition to the core evolution, the physical properties of the core, such as density and temperature, play an important role in determining the NH_3/N_2H^+ abundance ratio. In conclusion, in AFGl 5142 we found that the NH_3/N_2H^+ abundance ratio behaves differently to the low-mass case mainly because of the high temperature reached in hot cores.

References

Belloche, A., & Andé, P. 2004, A&A, 419, L35
Bergin, E. A., & Langer, W. D. 1997, ApJ, 486, 316
Beuther, H., & Henning, Th. 2009, A&A, 503, 859
Busquet, G., Palau, A., Estalella, R., et al. 2009, A&A, 506, 1183
Carpenter, J. M., Snell, R. L., & Schloerb, F. P. 1990, ApJ, 362, 147
Caselli, P., Myers, P. C., & Thaddeus, P. 1995, ApJ, 455, L77
Caselli, P., Benson, P., Myers, P. C., & Tafalla, M. 2002a, ApJ, 572, 238
Caselli, P., Walmsley, C. M., Zucconi, A., et al. 2002b, ApJ, 565, 344
Cesaroni, R., Felli, M., & Walmsley, C. M. 1999, A&AS, 136, 333
Chen, X., Launhardt, R., Bourke, T. L., & Barnes, P. J. 2008, ApJ, 683, 862
Chen, Y., Yao, Y., Yang, J., Zeng, Q., & Sato, S. 2005, ApJ, 629, 288
Collings, M. P., Dever, J. W., Fraser, H. J., McCoustra, M. R. S., & Williams, D. A. 2003a, ApJ, 583, 1058
Collings, M. P., Dever, J. W., Fraser, H. J., & McCoustra, M. R. S. 2003b, Ap&SS, 285, 633
Collings, M. P., Anderson, M. A., Chen, R., et al. 2004, MNRAS, 354, 1133
Daniel, F., Cernicharo, J., & Dubernet, M. -L. 2006, ApJ, 648, 461
Di Francesco, J., André, P., & Myers, P. C. ApJ, 617, 425
Eiroa, C., Torrelles, J. M., Miranda, L. F., Anglada, G., & Estalella, R. 1994, A&AS, 108, 73
Estalella, R., Mauersberger, R., Torrelles, J. M., et al. 1993, ApJ, 419, 698
Flower, D. R., Pineau des Forêts, G., & Walmsley, C. M. 2006, A&A, 456, 215
Fontani, F., Caselli, P., Crapsi, A., et al. 2006, A&A, 460, 709
Forveille, T., Guilloteau, S., & Lucas, R. 1989, CLASS Manual (Grenoble: IRAM)
Friesen, R. K., Di Francesco, J., Shimajiri, Y., & Takakuwa, S. 2010, ApJ, 708, 1002

Fuller, G. A., & Wootten, A. 2000, ApJ, 534, 854
Goddi, C., & Mosacadelli, L. 2006, A&A, 447, 577
Goddi, C., Moscadelli, L., Sanna, A., Cesaroni, R., & Minier, V. 2007, A&A, 461, 1027
Harju, J., Walmsley, C. M., & Wouterloot, J. G. A. 1993, A&AS, 98, 51
Hildebrand, R. H. 1983, QJRAS, 24, 267
Ho, P. T. P. 1977, Ph.D. Thesis, Massachusetts Institute of Technology
Ho, P. T. P., & Townes, C. H. 1983, ARA&A, 21, 239
Hotzel, S., Harju, J., & Walmsley, C. M. 2004, A&A, 415, 1065
Hunter, T. R., Testi, L., Taylor, G. B., et al. 1995, A&A, 302, 249
Hunter, T. R., Testi, L., Zhang, Q., & Sridharan, T. K. 1999, AJ, 118, 477
Jenness, T., Scott, P. F., & Padman, R. 1995, MNRAS, 276, 1024
Jørgensen, J. K. 2004a, A&A, 424, 589
Jørgensen, J. K., Schöier, F. L., & van Dishoeck, E. F. 2004b, A&A, 416, 603
Lee, J. -E., Bergin, E. A., & Evans, N. J. II 2004, ApJ, 617, L360
Matthews, B. C., Hogerheijde, M. R., Jørgensen, J. K., & Bergin, E. A. 2006, ApJ, 652, 1374
Palau, A., Estalella, R., Girart, J. M., et al. 2007, A&A, 465, 219
Palau, A., Sánchez-Monge, Á., Busquet, G., et al. 2010, A&A, 510, A5
Pirogov, L., Zinchenko, I., Caselli, P., Johansson, L. E. B., & Myers, P. C. 2003, A&A, 405, 639
Pirogov, L., Zinchenko, I., Caselli, P., & Johansson, L. E. B. 2007, A&A, 461, 523
Qiu, K., Zhang, Q., Megeath, S. T., et al. 2008, ApJ, 685, 1005
Rawlings, J. M. C., Harquist, T. W., Menten, K. M., & Williams, D. A. 1992, MNRAS, 255, 471
Reid, M. A., & Matthews, B. C. 2008, ApJ, 675, 1343
Sault, R. J., Teuben, P. J., & Wright, M. C. H. 1995, is Astronomical Data Analysis Software and Systems IV, ed. R. A. Shaw, H. E. Payne, & J. J. E. Hayes (San Francisco: ASP), ASP Conf. Ser. 77, 433
Snell, R. L., Huang, Y.-L., Dickman, R. L., & Claussen, M. J. 1988, ApJ, 325, 853
Sofia, U. J., & Meyer ,D. M. 2001, ApJ, 554, L221
Tafalla, M., Myers, P. C., Caselli, P., & Walmsley, C. M. 2004, A&A, 416, 191
Torrelles, J. M., Gómez, J. F., Anglada, G., et al. 1992, ApJ, 392, 616
Verdes-Montenegro, L., Torrelles, J. M., Rodríguez, L. F., et al. 1989, ApJ, 346, 193
Viti, S., & Williams, D. A. 1999, MNRAS, 310, 517
Viti, S., Caselli, P., Hartquist, T. W., & Williams, D. A. 2001, A&A, 370, 1017
Viti, S., Collings, M. P., Dever, J. W., McCoustra, M. R. S., & Williams, D. A. 2004, MNRAS, 354, 1141
Woodall, J., Agúndez, M., Markwick-Kemper, A. J., & Millar, T. J. 2007, A&A, 466, 1197
Zhang, Q., Hunter, T. R., Sridharan, T. K., & Ho, P.T.P. 2002, ApJ, 566, 982
Zhang, Q., Hunter, T. R., Beuther, H., et al. 2007, ApJ, 658, 1152
Zinchenko, I., Caselli, P., & Pirogov, L. 2009, MNRAS, 395, 2234